COMPUTATIONAL FLOW PREDICTIONS FOR HYPERSONIC DRAG DEVICES

Susan Tokarcik and Ethiraj Venkatapathy
Eloret Institute
Palo Alto, California

SUMMARY

The effectiveness of two types of hypersonic decelerators is examined: mechanically deployable flares and inflatable ballutes. Computational fluid dynamics (CFD) is used to predict the flowfield around a solid rocket motor (SRM) with a deployed decelerator.The computations are performed with an ideal gas solver using an effective specific heat ratio of 1.15. The results from the ideal gas solver are compared to computational results from a thermo-chemical nonequilibrium solver. The surface pressure coefficient, the drag, and the extent of the compression corner separation zone predicted by the ideal gas solver compare well with those predicted by the nonequilibrium solver. The ideal gas solver is computationally inexpensive and is shown to be well suited for preliminary design studies. The computed solutions are used to determine the size and shape of the decelerator that are required to achieve a drag coefficient of 5. Heat transfer rates to the SRM and the decelerators are predicted to estimate the amount of thermal protection required.

NOMENCLATURE

A	reference area, $A = \pi R_{case}^2$
C_D	drag coefficient, $C_D = D/(q_\infty A)$
C_H	heat transfer coefficient, $C_H = q_w / (0.5\rho_\infty U_\infty^3)$
M	total mass, kg
q_∞	freestream dynamic pressure, N/m^2
q_w	wall heat transfer rate, W/cm^2
R_{case}	radius of SRM casing
U_∞	freestream velocity, m/s
β	ballistic coefficient, $\beta = M/(C_D A)$, kg/m^2
δ	flare angle or initial angle of ballute
γ	specific heat ratio, c_p/c_v
ρ_∞	freestream density, kg/m^3

INTRODUCTION

The Aeroassist Flight Experiment (AFE) is designed to provided information which is needed to design a full scale Aeroassist Space Transfer Vehicle (ASTV). The ASTV will be used to transfer payload from high Earth orbits, lunar bases, and planetary missions to low Earth orbit (LEO). In order to enter LEO the ASTV will enter Earth's upper atmosphere and use aerobraking to attain the

necessary velocity depletion. It will then fly back out of the upper atmosphere and enter LEO. Because the ASTVs will operate at very high altitudes, the flow about the ASTV may be in thermo-chemical nonequilibrium. These conditions cannot be adequately simulated in ground based facilities. Therefore a flight experiment, the AFE, is required.

The AFE is a subscale ASTV. The AFE would fly a representative ASTV trajectory in order to collect the desired flight data. The AFE would be deployed from the Space Shuttle. Then a solid-propellant rocket motor (SRM) is fired to accelerated the AFE. When the desired entry velocity for the test is attained, the SRM casing is jettisoned from the AFE, and the AFE continues on to perform an aerobraking maneuver. This scenario is shown in figure 1.
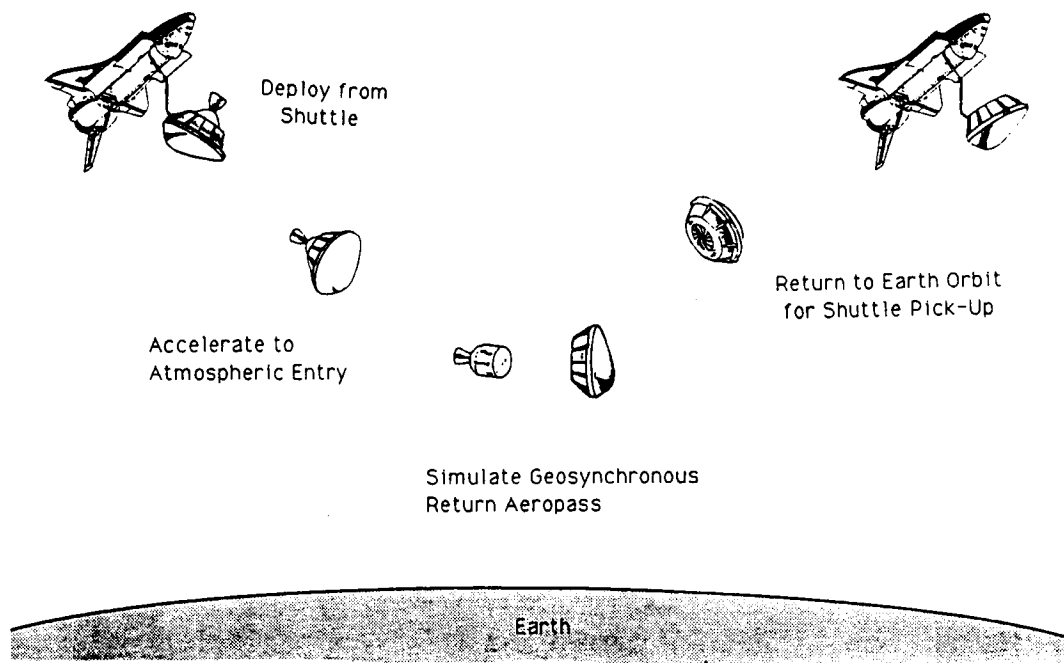

Figure 1. AFE mission (NASA I-87-9597).

The SRM casing jettisoned from the AFE is large enough that it will not entirely burn up during entry. To protect human beings from this falling debris, it is required that the SRM casing drop in to the water at least 300 miles from any large land mass (ref. 1). In order to determine approximately where the SRM casing will land, it is necessary to know where it begins its descent into the atmo-sphere. If the SRM casing initially skips out of the atmosphere before being captured, it is very difficult to predict where and when it will be captured and where it will finally land. As recently as April 1991, the seriousness of such a problem was brought to light when a large piece of debris from a Soviet space station fell into a populated area of Argentina.

Whether or not the SRM casing will skip out is determined by its ballistic coefficient, $\beta = M/(C_D A)$. The reference area, A, used to calculate C_D is the same as that used to calculate β. Therefore, β is altered by changing the total mass of a body or the total drag produced by a body. Increasing the drag, hence lowering β, will cause a body to lose momentum more quickly. This will cause the body's atmospheric trajectory to become steeper. Increasing the mass of a body, hence

increasing β, will tend to cause the body to decelerate more slowly and to maintain a shallower trajectory longer. It is this shallow trajectory that can cause a body to skip out.

The calculated trajectories for a range of ballistic coefficients is shown in figure 2 (ref. 2). The ballistic coefficient of the SRM casing is approximately 112 kg/m^2. As can be seen in figure 2, a body with a β of 112 has a high probability of skipping out before being captured by the atmosphere. Also shown in figure 2 is a range of acceptable ballistic coefficients. A ballistic coefficient of 49 kg/m^2 will assure that skip out does not occur. In order to lower β, either the weight of the SRM casing must be lowered or the drag must be increased. Since the minimum weight of the SRM casing is predetermined by the needs of the AFE mission, it cannot be adjusted to lower β. Therefore, the drag must be increased. The C_D of the SRM casing alone is predicted to be approximately 1.56. By increasing the C_D to around 5, a β of 49 or less can be attained. The additional drag needed can be produced by attaching a drag enhancement device to the SRM casing to increase the total pressure drag.
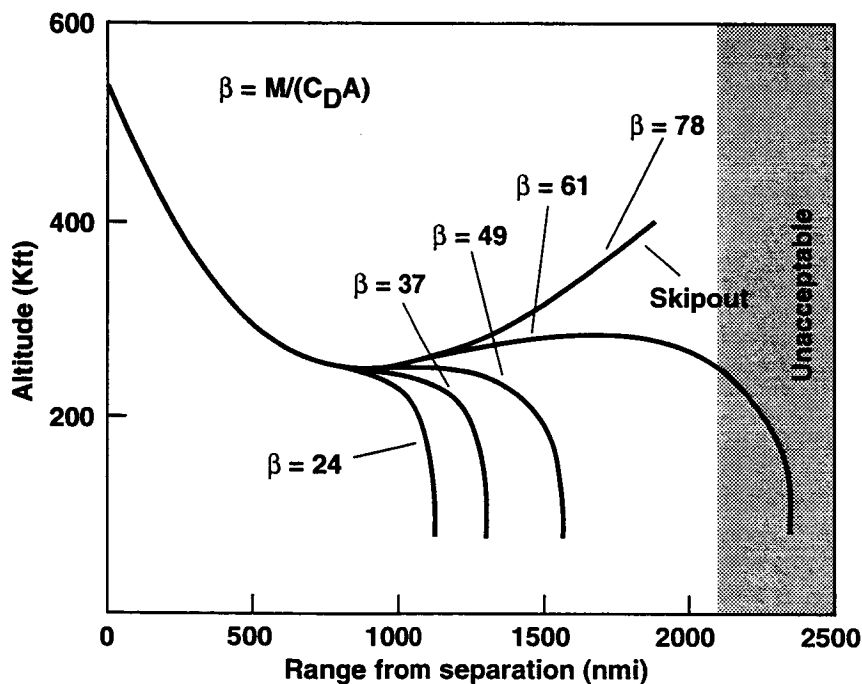

Figure 2. Ballistic entry trajectories (ref. 2).

The use of high speed and hypersonic drag brakes, has been investigated for many years and many different configurations have been proposed. Among these drag devices were attached or tethered ballutes (ref. 3). A ballute is a combination balloon parachute and is inflated using ram air pressure or an on board pressure source. Also investigated were rigid flares, spoilers, and spikes that are mechanically deployed (ref. 4). A flare is attached around the entire vehicle while one or more spoilers can be deployed intermittently around the vehicle. Most recently, a ballute decelerator has been examined computationally (ref. 2). Most of the research done thus far for hypersonic decelerators has been applicable to high performance reentry vehicles or Apollo capsule recovery, payload

recovery, and booster payload collision avoidance. However, none of this research takes into account the real gas effects encountered at the altitudes and speeds experienced by the SRM casing.

A number of considerations must be taken into account when choosing a viable decelerator configuration. These considerations include high heating rates, ease of decelerator deployment, stability of the SRM/decelerator configuration, and, ultimately, how much drag the decelerator can produce. After examining several of the above configurations, it was decide that a ballute attached to the rear of the SRM casing or a flare attached in the same manner would most likely be the best suited for this mission (ref. 1). This conclusion was reached for the following reasons. First, a ballute attached to the rear of the SRM casing or a conical flare attached in the same way would tend to be a more stable configuration. Also, since the flare is mechanically deployed, tumbling would not affect the flare deployment. If an on board pressure source is used to inflate the ballute, tumbling would not affect the ballute deployment. The amount of drag produced by the conical flare and the ballute must be predicted in order to determine the size of the drag device needed to produce the desired increase in drag. Also the heat transfer rates to these drag devices needs to be estimated in order to determine whether existing materials could be used for thermal protection.

NUMERICAL METHODS

Thermo-Chemical Nonequilibrium Solver

The actual configuration for the SRM casing is shown in figure 3(a). Shown in figure 3(b) is the modified SRM configuration, with an attached flare decelerator, used in the numerical computations. The model for the ballute is shown in figure 3(c). The outer ring of the SRM casing shown in figure 3(a) is neglected in the models used for numerical computations. Neglecting the ring is possible because it will be contained within the large separated region of the flow. Because of this, the ring is not important when calculating the total drag. Therefore, the ring is neglected in the computational analysis.

All flowfield calculations assumed axisymmetric flow. The freestream conditions for the computations correspond to the peak heating trajectory point (ref. 1). These conditions are given in table 1. Because of the high altitude and the high speed of the SRM trajectory, the flowfield around the SRM casing may be in thermo-chemical nonequilibrium. This flowfield was solved for by using a thermo-chemical nonequilibrium code developed by Palmer. This code is an explicit, finite-difference, shock-capturing algorithm that used flux-vector splitting to solve the thin layer Navier-Stokes equations in a time marching fashion (ref. 5). The algorithm incorporated a finite rate chemistry model consisting of 10 species and a fully coupled two temperature thermal nonequilibrium model of Park (ref. 6). This code has been validated using experimental and computational data. The experimental data included ballistic range, shock tunnel, and flight data. The computational results have been compared against values from a thermo-chemical nonequilibrium solver developed by Candler. This code also solved the thin layer Navier-Stokes equations but used a finite volume, fully coupled, implicit technique that used Gauss-Seidel line relaxation (ref. 7). It also incorporated a multi-temperature thermal nonequilibrium model. However, the nonequilibrium codes are very costly to run, requiring 3 to 4 hours of CPU time on a CRAY-2 for the cases considered in this work. Therefore, they are not well suited for producing results for multiple configurations as was required here.
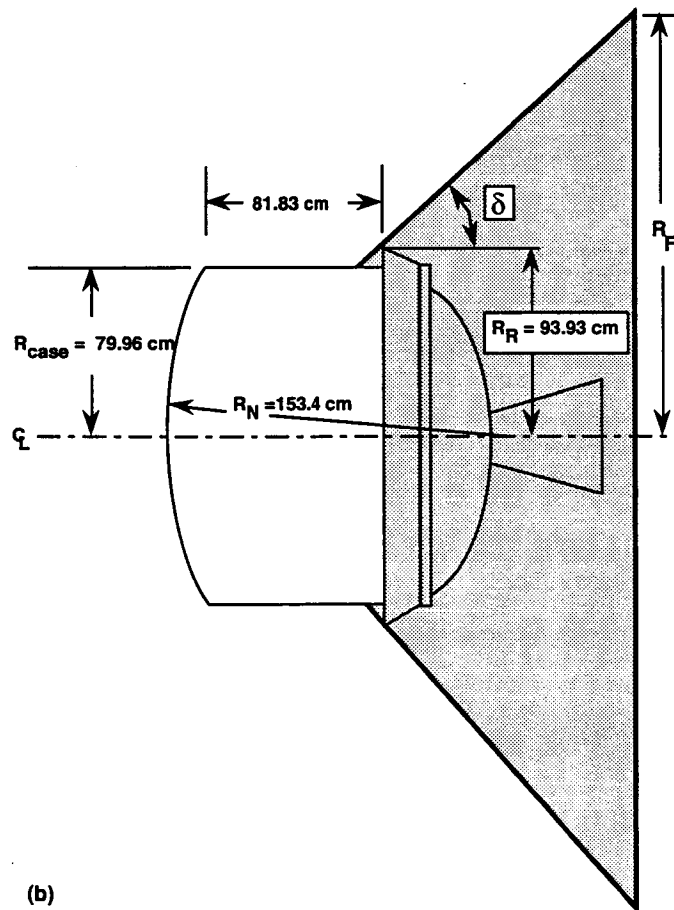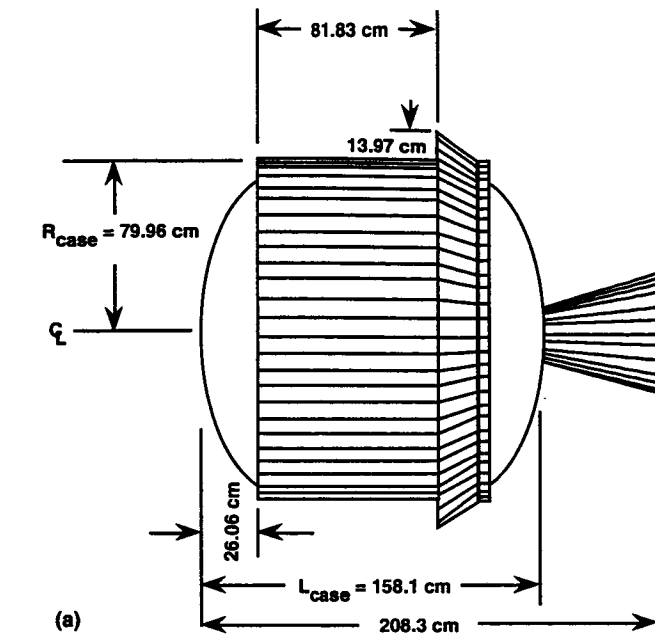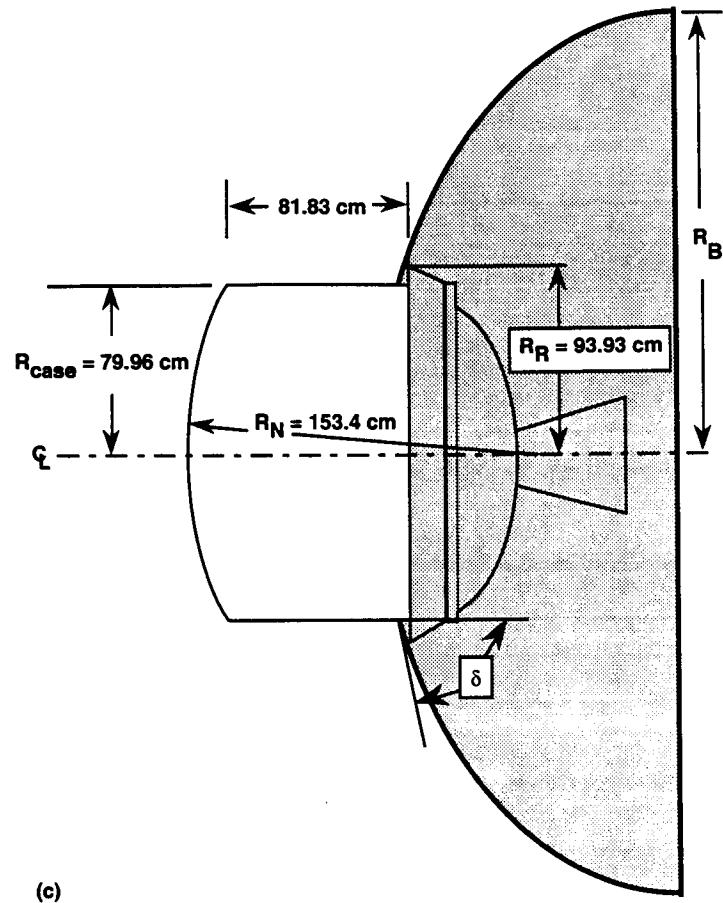
Figure 3. SRM model. (a) Configuration, (b) model for computation with flare.

149

(c)

Figure 3. Concluded. (c) Model for computations with ballute.

Table 1. Freestream conditions

altitude	76,250 m
velocity	9,126 m/s
density	3.6087×10^{-5} kg/m^3
pressure	2.0674 N/m^2
temperature	199.6 K
Reynolds No.	22,370 /meter

Effective γ Ideal Gas Solver

In order to calculate solutions in a timely manner, a perfect gas version of the thermo-chemical nonequilibrium code developed by Candler was used. An effective specific heat ratio, γ, was used in the ideal gas solver in an effort to simulate the real gas nature of the flowfield. This technique has been used successfully to predict drag and moment coefficients produced by a body in a real gas flowfield (ref. 8). The choice of effective γ was based on a solution produced by Palmer's thermo-chemical nonequilibrium solver. Further explanation of the procedure used to choose an effective γ

150

is given in the next section. The ideal gas solver has been validated against experimental data for spheres, sphere cones, and sharp nosed cones at a variety of hypersonic speeds (ref. 7). The ideal gas solver is very robust and requires only 10 to 15 minutes of CPU time on a CRAY-2 for the same conditions that were used in the nonequilibrium code.

A schematic of the expected flow features of the SRM casing with a conical flare decelerator is shown in figure 4. Shown in this figure is the strong outer blunt body shock produced by the nose of the SRM casing. Then there is a strong expansion region around the shoulder of the SRM casing. The juncture of the SRM casing and the decelerator forms a compression corner. The hypersonic flow in this region cannot negotiate this corner and separates. A shock forms at the upstream edge of the separated region. Further downstream, this shock interacts with the blunt body shock off the nose of the SRM. The peak pressure and heat transfer rate for the drag device occur in the vicinity of this shock-shock interaction. The two shocks then coalesce to form an oblique shock.

While both the nonequilibrium solver and the perfect gas solver have been used extensively for hypersonic blunt body flows, until now neither has been used to study flows with large separated regions such as that shown in figure 4. The prediction of this separated region is important since the size of the region will affect the amount of drag produced by the decelerator.
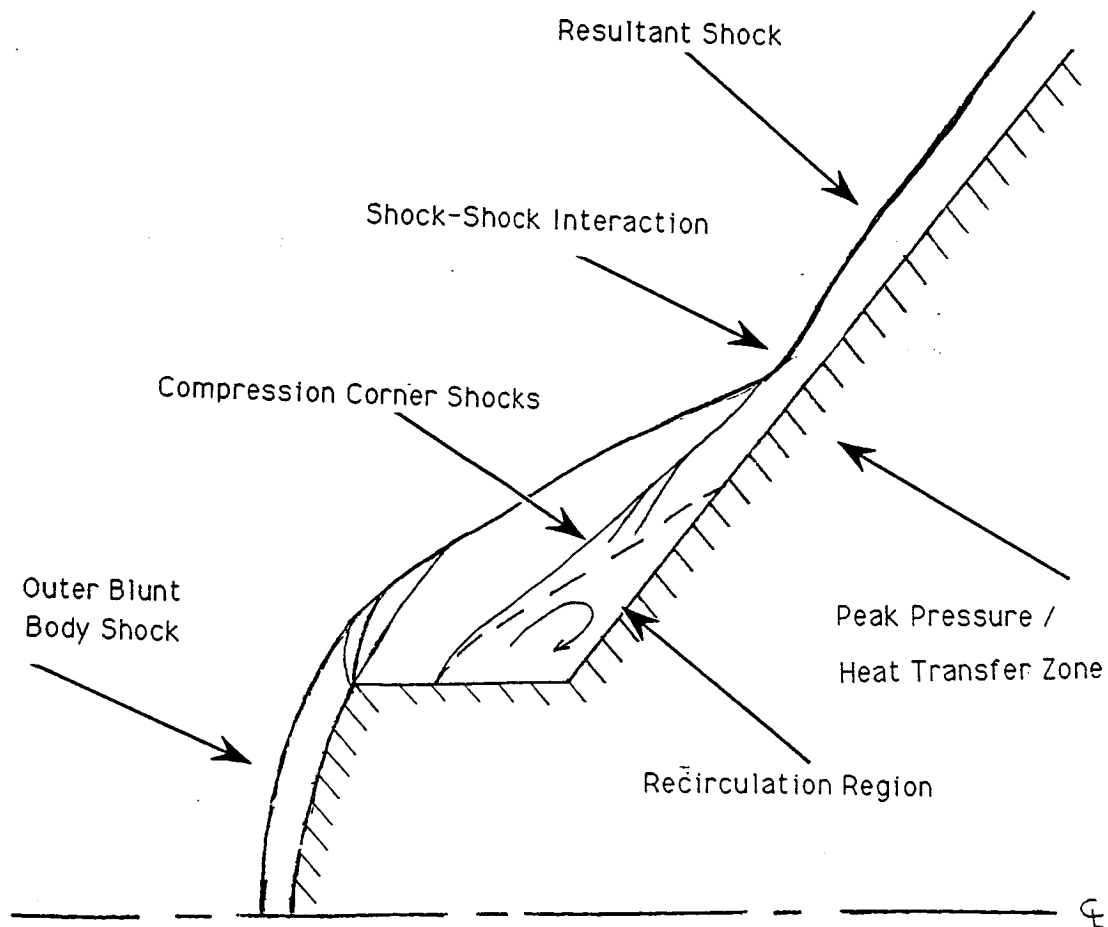
Figure 4. Flow schematic for SRM and flare.

151

COMPUTATIONAL RESULTS AND ANALYSIS

2-D Compression Corner Simulation

The region where the the SRM casing and the decelerator join forms a compression corner. The hypersonic flow coming into this compression region cannot negotiate the corner made by the SRM/decelerator juncture, and the flow separates. In order to confirm that this type of flow can be predicted with reasonable accuracy using the available solvers, a comparison is made with experimental results for a two-dimensional compression corner (ref. 9). The experimental flow was laminar until the reattachment region where transition was suspected to have occurred. The experimental case used for comparison was a compression corner with a 15° corner angle at Mach 10 with a 100°K constant temperature surface. The experiment was performed in air with $\gamma = 1.4$. The freestream conditions were as follows: $T_\infty = 50°$ K, $P_\infty = 294.5$ Pa, $Re_L = 2.3 \times 10^6$ where L is the length of the flat plate portion of the model, L = 0.25 m. The solution computed using the ideal gas solver with $\gamma = 1.4$ is compared to the experimental schlieren photograph in figures 5(a) and 5(b). In figures 6 and 7, C_P and C_H are compared with experimental results. In figure 6, the modest pressure rise at about X/L = 0.82 indicates the separation point. This is followed by a plateau typical of laminar separation (ref. 9). Then, in the reattachment region, the pressure rises rapidly and over-shoots the constant downstream value. The pressure over-shoot occurs in the reattachment region and is a common feature in high Mach number separated flows (ref. 10). This over-shoot is caused by the interference between the separation and reattachment shock waves. The computational results are able to predict the pressure overshoot in the reattachment region. The overshoot predicted by the computations is somewhat less than that found by experiment. The discrepancy could be due to turbulent transition taking place in this area. The differences in peak pressure are acceptable and any impact on the decelerator calculations will not be significant. The computed C_P in the separated region compared well with experimental values. The size of the separated region and the value of the pressure within the separated region agreed with that found experimentally.

Heat transfer data are shown in figure 7. The experimental data show that heat transfer rates decrease slowly along the upstream portion of the flat plate. The separation point is indicated by the sharp decrease in heat transfer rate. The heat transfer rate reaches a minimum within the separated
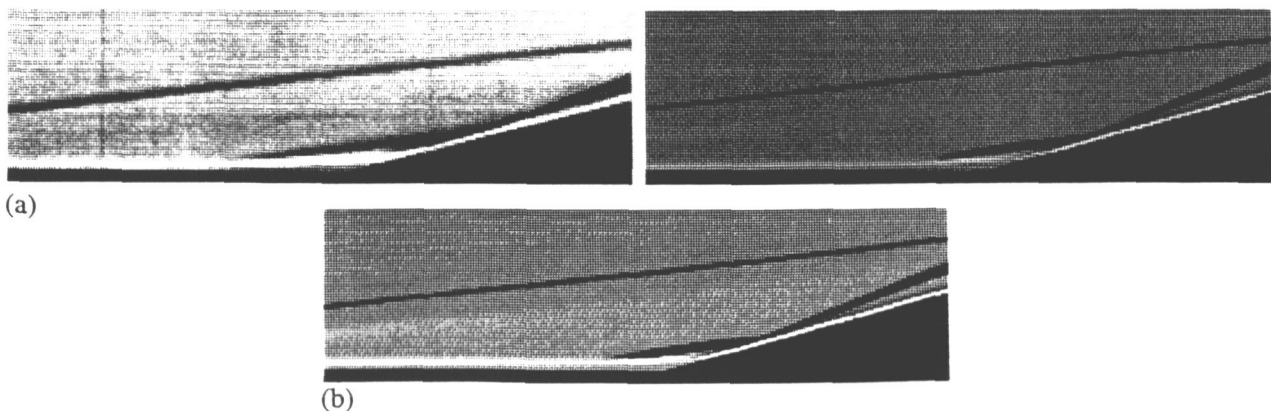

(a)

(b)

Figure 5. (a) Schlieren of 2-D compression corner (ref. 9), (b) calculated Schlieren of computational solution.
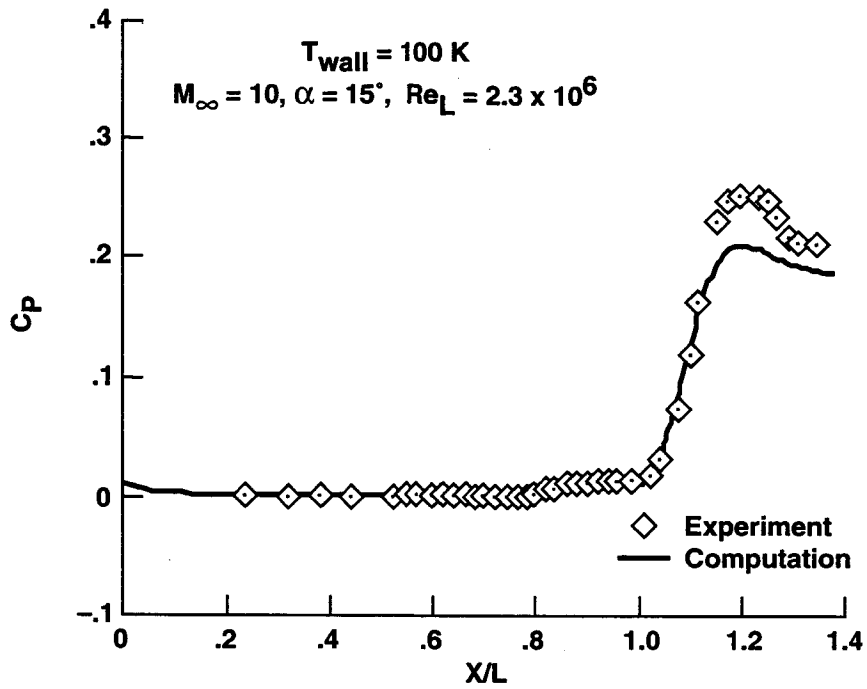
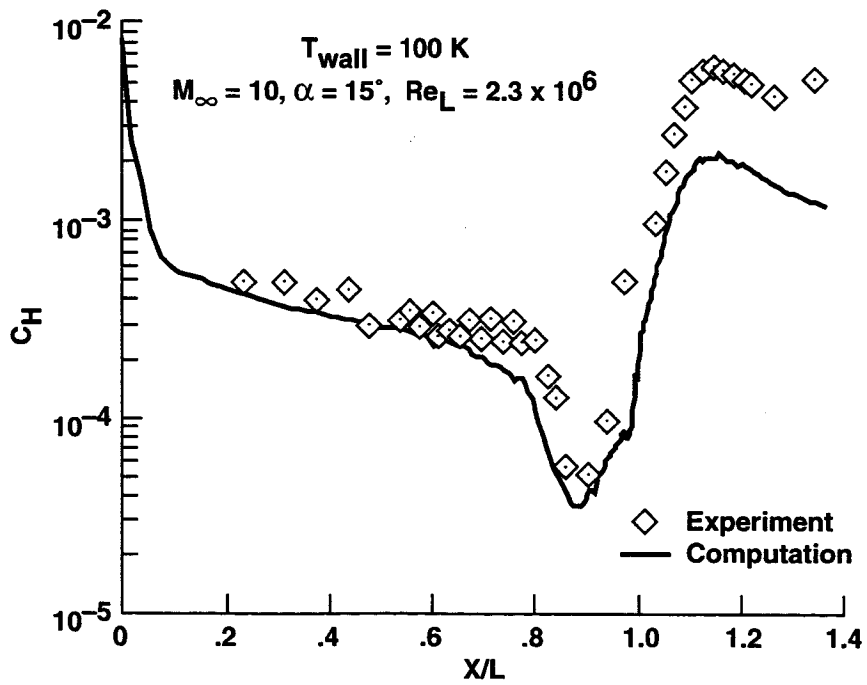Figure 6. Pressure coefficient for 2-D compression corner.

Figure 7. Heat transfer rates for 2-D compression corner.

region and then increases rapidly in the reattachment region. The trend of the computed heat transfer rates compares well with the experiment. The size and location of the separated region, inferred by the rapid drop and then rapid rise in heat transfer, is adequately predicted by the computational methods. The computed heat transfer rates reach a peak in the reattachment region but fall short of the experimental peak value. However, the agreement is adequate for preliminary design purposes. The higher heat transfer rates found by the experiment may be due to transition taking place in the reattachment region.

SRM/DECELERATOR SIMULATIONS

Although the flowfield around the SRM/decelerator will be dominated by real gas effects, the pressure field can be simulated using a perfect gas with an effective γ. The value of the effective γ that is chosen depends on the particular conditions under consideration. In a hypervelocity flow of a diatomic gas, high temperatures cause the molecules to dissociate into atoms, and the available modes of energy decrease from five to three, namely translational energy in three dimensions. Decreasing the available energy modes will increase the value of γ until the theoretical limit of 5\3 is reached. However, the high temperatures also cause the molecules to become vibrationally excited. This increases the number of energy modes and thus decreases γ. For a highly nonequilibrium flow-field, vibrational energy modes are excited, but the molecules do not have time to dissociate into atoms. So the chemical dissociation effects are swamped by the thermal effects, and the value of γ drops below the perfect gas value of 1.4. Flowfields which are dominated by real gas effects may have a value of γ around 1.1.

The pressure field can be simulated with a perfect gas solution because the pressure is only loosely coupled to the thermo-chemistry of the flow. Instead it is much more dependent on the fluid dynamics of the flow. It was shown earlier that the blunt body flow and the compression corner flow for the SRM/decelerator can be calculated with reasonable accuracy. Therefore, with the proper choice for the value of effective γ, the pressure field for this flow can be calculated reasonably well.

To be able to choose an appropriate effective γ either a computational solution which takes into account the real gas thermo-chemistry or experimental data for the flight conditions in question is needed.Since no experimental data exists for the present configuration, the nonequilibrium code is used to generate the real gas flowfield around the SRM/decelerator configuration. The nonequilibrium code is used to determine the shock shape and standoff distance associated with the real gas flow. The shock shape and standoff distance determine the pressure field of the flow. A series of effective γs was tried in the ideal gas solver in the effort to reproduce the real gas shock shape and standoff distance. The resulting drag curves for various γs is shown in figure 8. This figure shows that an effective γ of 1.15 does a good job of reproducing the surface pressure field.

Pressure contours of the entire flowfield are shown in figure 9. The pressure contours computed by the real gas solver for an SRM with a 50° flare are shown in figure 9(a). Figure 9(b) shows the pressure contours computed by the ideal gas solver with an effective γ of 1.15 for the same configuration. Figures 9 and 10 show that an effective γ of 1.15 does a very good job of reproducing the pressure field of the real gas flow.
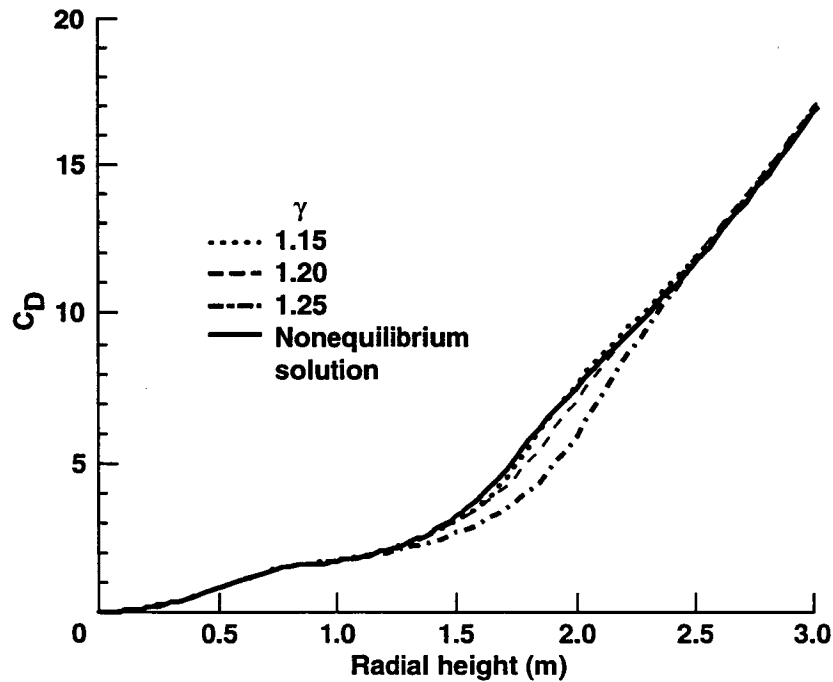
Figure 8. Drag coefficient for variable γ and real gas solution.

The pressure contours shown in figure 9 can be compared to the schematic of the expected flow features shown in figure 4. The pressure contours clearly show the blunt body shock formed by the nose of the SRM casing. The shock formed at the separation point is seen as a moderately large gradient in pressure just downstream of the SRM shoulder expansion. The separation shock interacts with the bow shock creating a high pressure region about half way up the flare. The two shocks merge in the interaction region to form an oblique shock. The extent of the separation region can be inferred from the pressure contours as the region of nearly constant pressure at the base of the SRM casing. A better idea of the separated region can be made by looking at velocity vectors. Figure 10 shows an expanded view of the SRM/decelerator corner region. The velocity vectors clearly show that a large portion of the SRM casing and the flare are contained within the separated region.

Computations for Conical Flare Decelerators

With an appropriate value of γ, the perfect gas code was used to study the flare and ballute drag devices. The decelerator must increase the drag of the SRM casing such that $\beta = 49$ Kg/m^2 or less is achieved. This condition corresponds to producing a C_D of about 5.

The first decelerator concept that was examined was the conical flare. A schematic of the flow-field produced by this type of configuration is shown in figure 4. The schematic was drawn for a flare angle of 50°. The angle of the flare influenced the size of the separated region and also the shape and strength of the shock in the downstream region. The size of the separated region affects the efficiency of the flare. If no separation occurs, the entire length of the flare is utilized as a compression surface. If a separation region exists, that portion of the flare within the separated region is
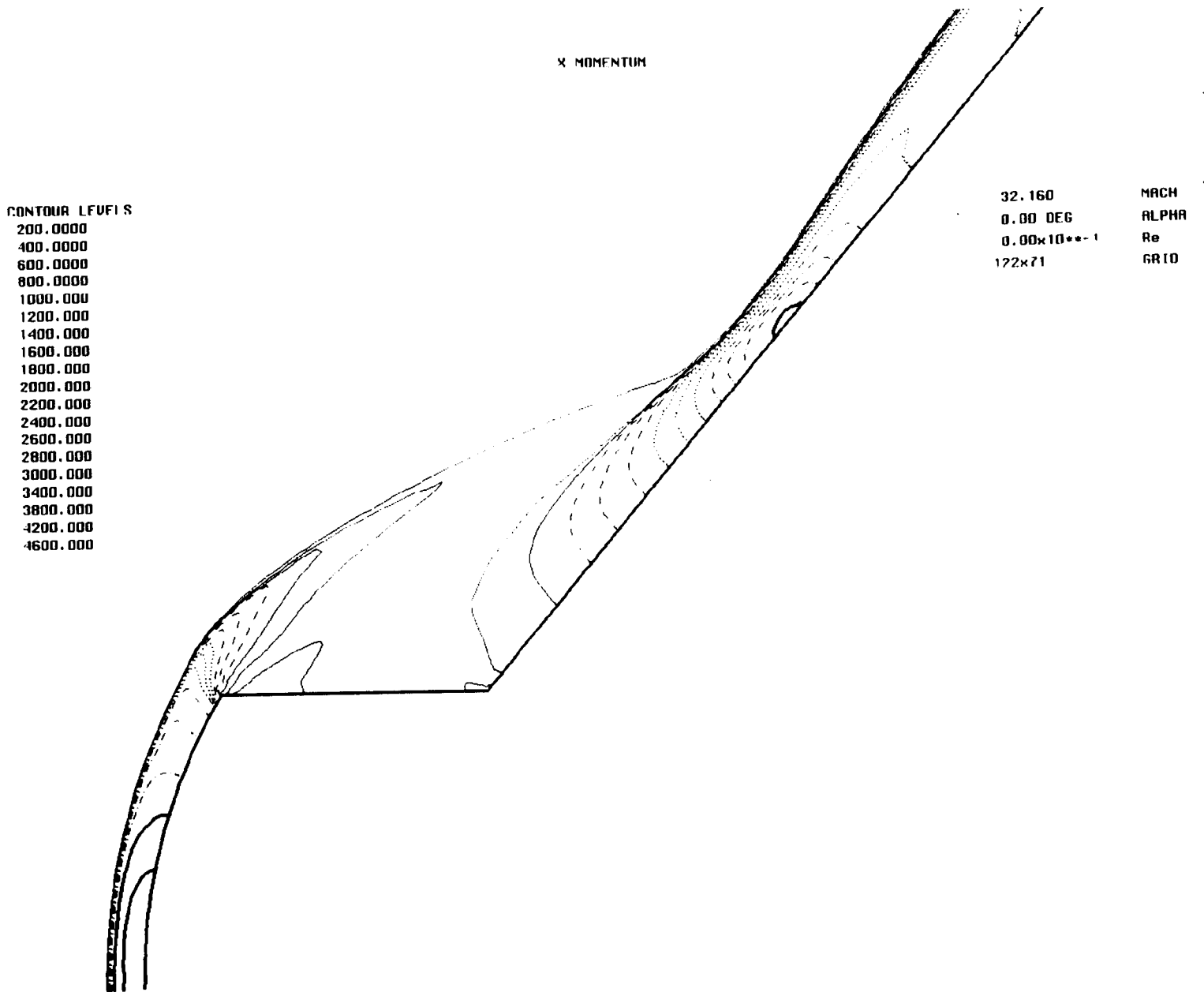
X MOMENTUM

CONTOUR LEVELS
200.0000
400.0000
600.0000
800.0000
1000.000
1200.000
1400.000
1600.000
1800.000
2000.000
2200.000
2400.000
2600.000
2800.000
3000.000
3400.000
3800.000
4200.000
4600.000

32.160   MACH
0.00 DEG   ALPHA
0.00x10**-1 Re
172x71   GRID

Figure 9. Pressure contours. (a) Real gas solution.

156

X MOMENTUM

CONTOUR LEVELS
200.0000
400.0000
600.0000
800.0000
1000.000
1200.000
1400.000
1600.000
1800.000
2000.000
2200.000
2400.000
2600.000
2800.000
3000.000
3400.000
3800.000
4200.000
4600.000

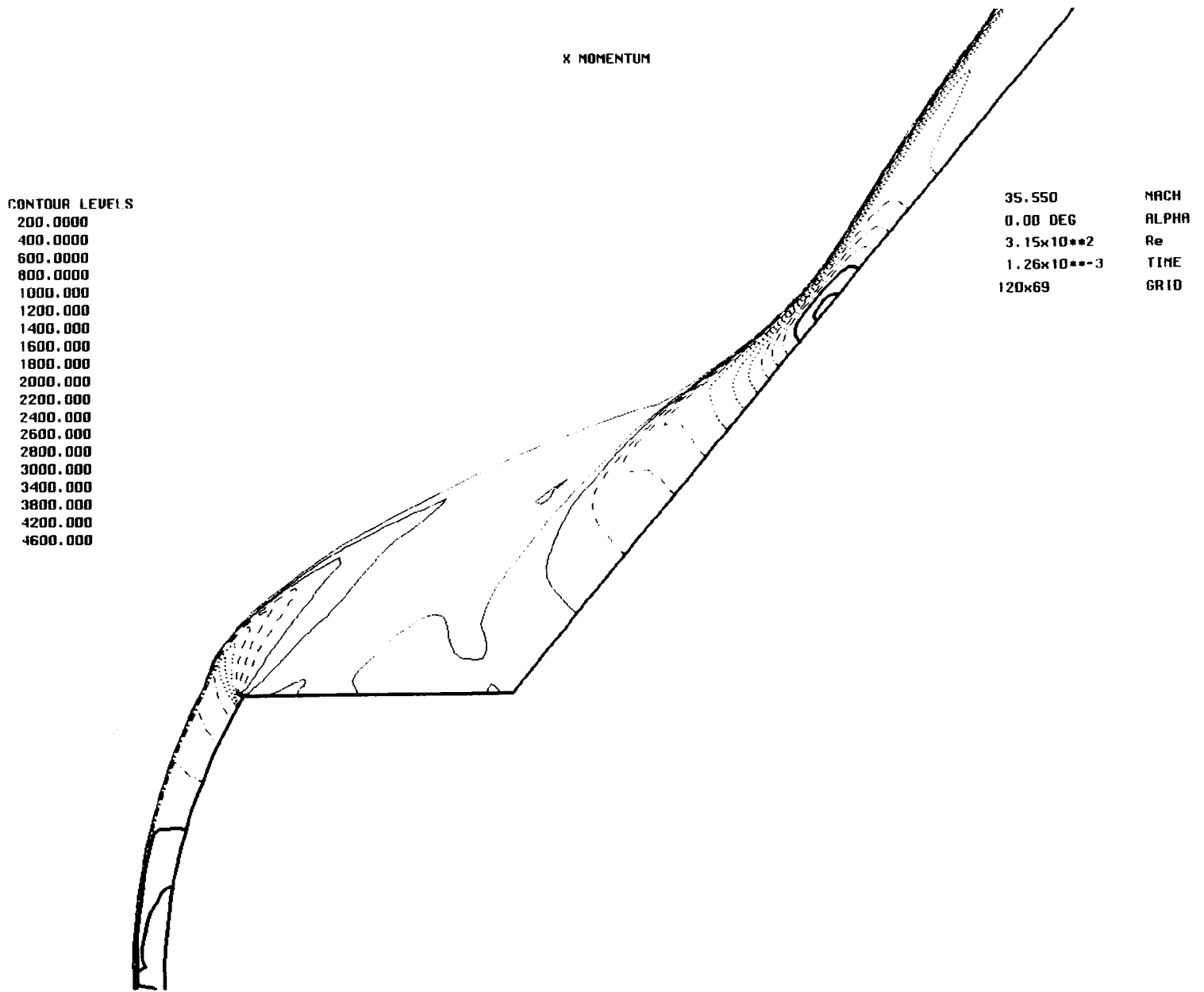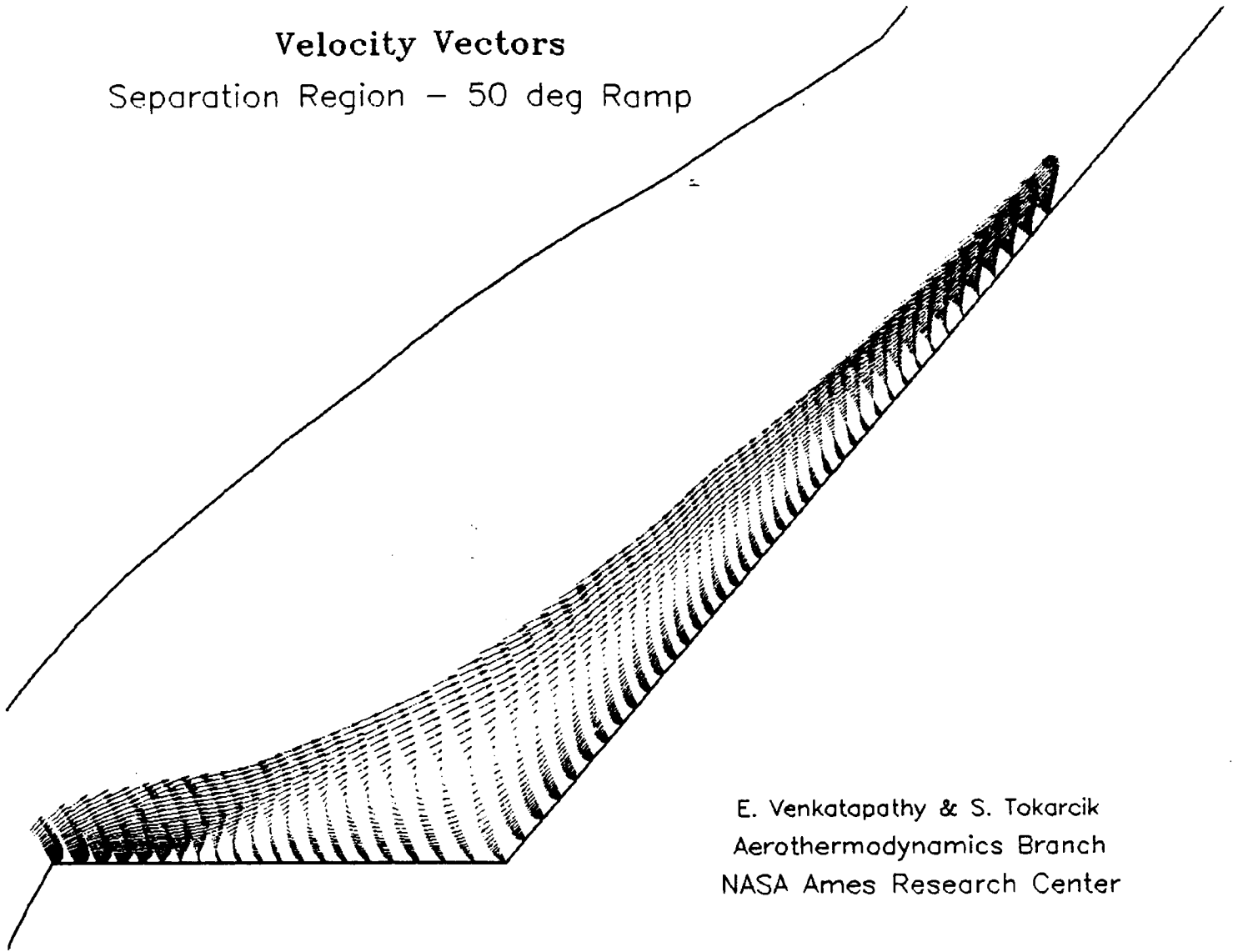| 35.550 | MACH |
0.00 DEG	ALPHA
3.15x10**2	Re
1.26x10**-3	TIME
120x69	GRID

Figure 9. Concluded. (b) $\gamma = 1.15$.

Velocity Vectors

Separation Region — 50 deg Ramp

E. Venkatapathy & S. Tokarcik
Aerothermodynamics Branch
NASA Ames Research Center

Figure 10. Velocity vectors – separation region 50° flare with $\gamma = 1.15$.

lost as a compression surface. The strength of the shock produced by the flare also affects the efficiency of the decelerator. A strong shock produces a greater pressure rise than a weak shock and therefore a greater increase in drag. Also, for larger flare angles, a greater portion of the pressure force vector acting on the body is directed in the axial, or drag, direction. Therefore, more drag is produced for the same distribution of surface pressure.

Pressure contours for three flare angles, 40°, 50°, and 60°, were computed. The results for the 50° flare are shown in figure 9(b). The 40° and 60° cases are shown in figures 11(a) and 11(b). A very small separation region was produced by the 40° flare, and a relatively weak downstream shock was formed. The peak pressure on the flare for this case was considerably lower than at the SRM nose stagnation point. The 50° flare produced a larger separated region and a stronger resulting oblique shock. The peak pressure produced by this flare was on the order of that produced in the

SRM nose region. As the flare angle was increased to 60° the character of the downstream shock changed. A very large separated region was produced encompassing almost the entire SRM casing downstream of the expansion shoulder. But more importantly, the downstream shock changed from a weak oblique shock to a strong blunt shock. The peak pressure on the flare occurs in the area where the strong shock is located. This pressure was much higher than the SRM nose stagnation point pressure. The C_D produced by the 40°, 50°, and 60° flares is shown in figure 12 . As can be seen in this figure, the desired C_D of 5 can be achieved by any of these flares with the proper choice ramp length.
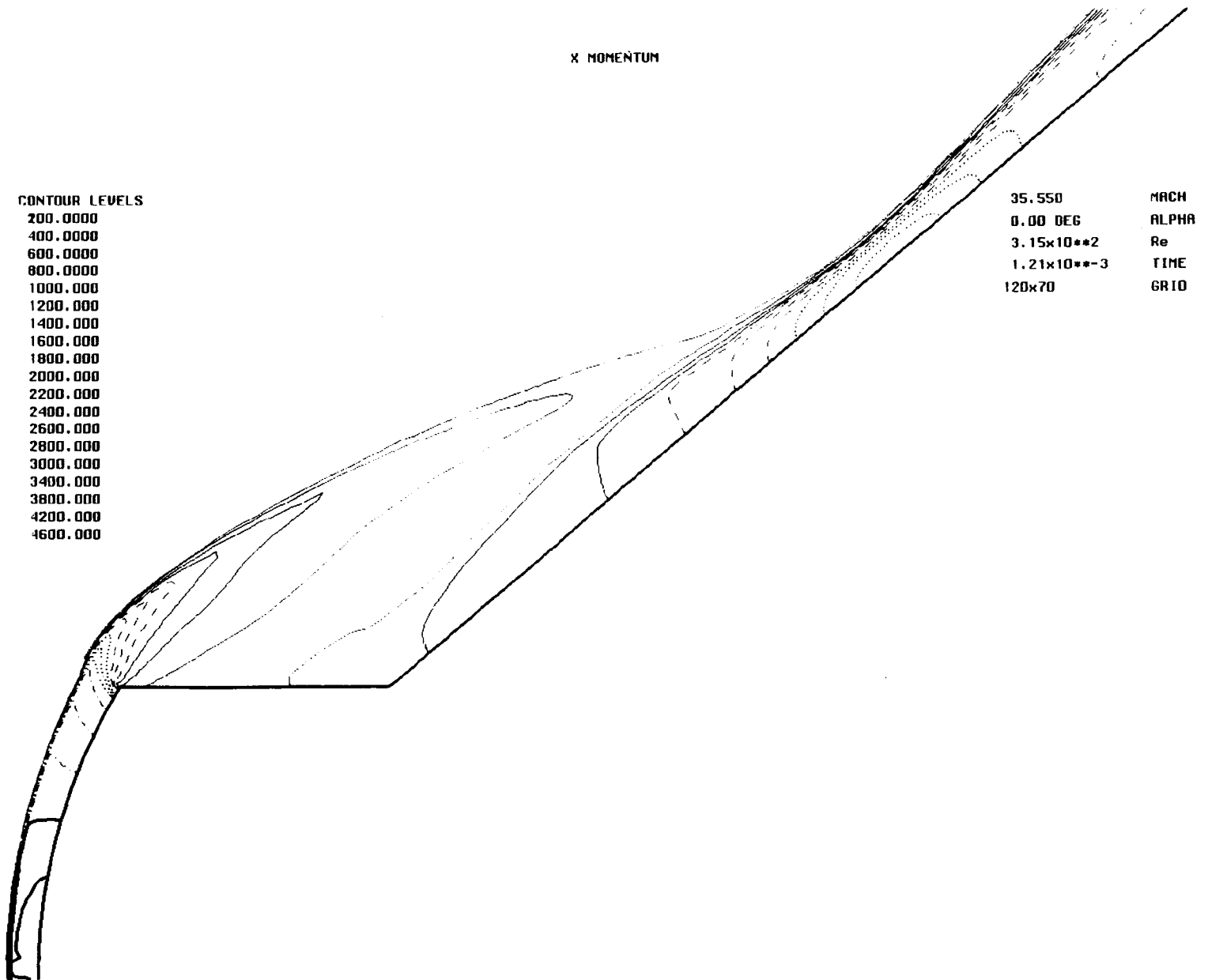
X MOMENTUM

CONTOUR LEVELS
200.0000
400.0000
600.0000
800.0000
1000.000
1200.000
1400.000
1600.000
1800.000
2000.000
2200.000
2400.000
2600.000
2800.000
3000.000
3400.000
3800.000
4200.000
4600.000

35.550	MACH
0.00 DEG	ALPHA
3.15×10^{2}	Re
1.21×10^{-3}	TIME
120×70	GRID

Figure 11. Pressure contours. (a) 40° flare.

X MOMENTUM

CONTOUR LEVELS
200.0000
400.0000
600.0000
800.0000
1000.000
1200.000
1400.000
1600.000
1800.000
2000.000
2200.000
2400.000
2600.000
2800.000
3000.000
3400.000
3800.000
4200.000
4600.000

35.550   MACH
0.00 OEG   ALPHA
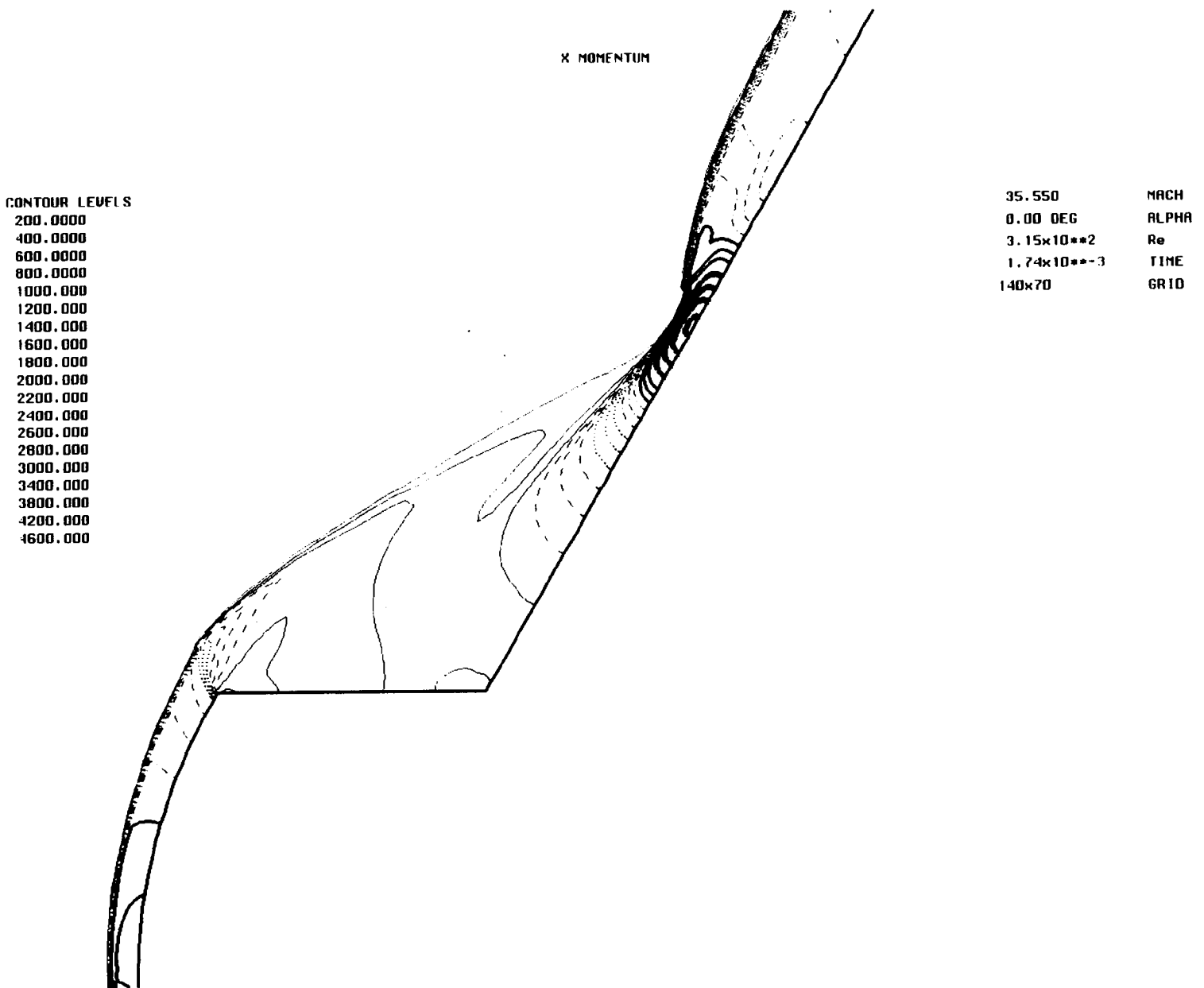3.15x10**2   Re
1.74x10**-3   TIME
140x70   GRID

Figure 11. Concluded. (b) 60° flare.

The computed heat transfer rates for the flare decelerators are shown in figure 13 . The rise in surface heat transfer rate seen at 0.9 m along the surface was due to the thinning of the boundary layer as the flow expanded around the shoulder of the SRM casing. The peak in heat transfer rate to the flare was due to the bow shock, produced by the nose of the SRM, interacting with the shock produced by the decelerator. The peak in heat transfer rate corresponds to the peak pressure on the flare. This region of peak pressure can be seen in the pressure contours shown in figure 11. The peak in heat transfer rate on the flare was of particular importance because, for a ballistic coefficient of 49, the decelerator must survive for approximately 150 seconds to ensure atmospheric capture.
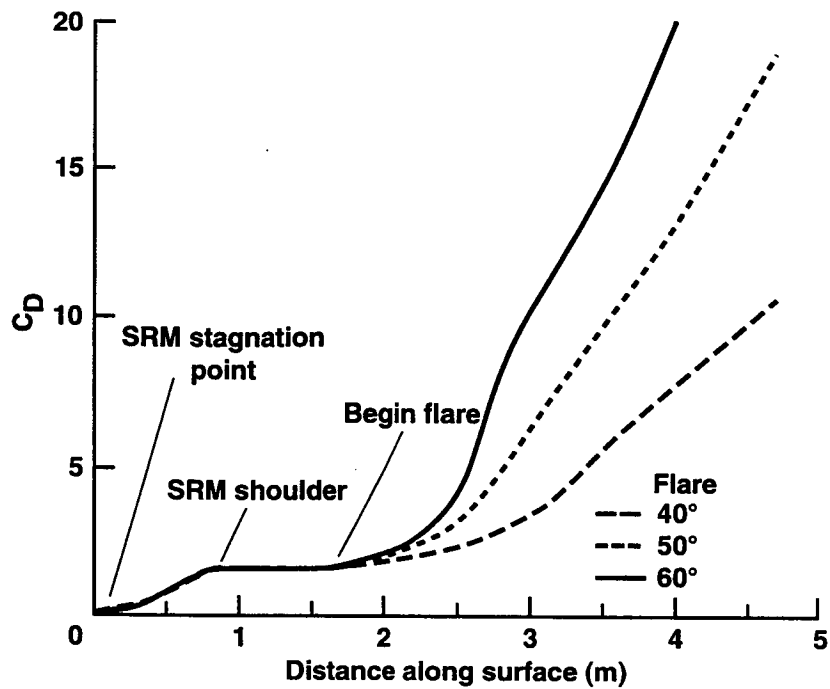
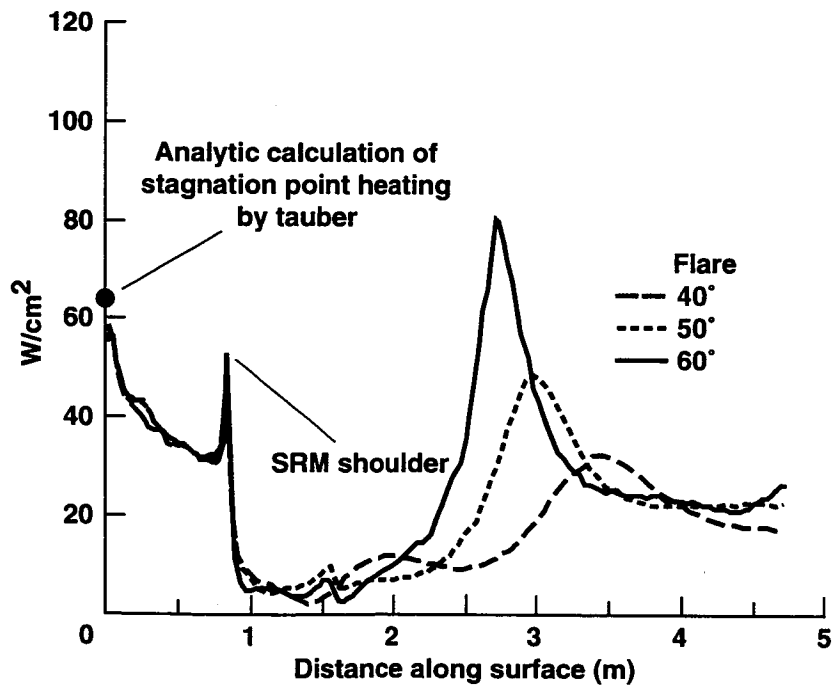Figure 12. Drag coefficient for flare.

Figure 13. Heat transfer rates for flare.

While the 40° flare has a low heat transfer rate, figure 13, it must have a greater length than the 50° or 60° flares in order to achieve the desired C_D, figure 12. Therefore, an additional mass penalty must be accepted. The 60° flare can achieve the desired drag with a relatively short length, but it

must also endure a significantly higher heat transfer rate than the other configurations. This brings the survivability of the 60° flare into question. The 50° flare achieved a C_D of 5 with a length only 20% larger then the 60° case. Furthermore, the 50° flare had a peak heat transfer rate similar to that found at the stagnation point and shoulder of the SRM casing which was considerably lower than for the 60° flare. An analytical check of the SRM stagnation point heating rate was performed by Tauber using reference 10. This point, shown in figure 13, is only 8% higher than that calculated by the perfect gas solver.

Computations for Ballute Decelerators

The next type of drag device that was examined was the ballute. The ballutes studied here are ellipsoidal in shape. The ballutes were attached to the SRM casing with initial angles that varied between $\delta = 70°$ and $\delta = 80°$. The ballute produced a bow shock wave that interacted with the bow shock off the nose of the SRM casing. This is in contrast to a flare drag device which generally produced a weaker oblique shock. The interaction of the SRM nose shock and the ballute shock created a high pressure region on the surface of the ballute. Downstream of this region the pressure dropped off as the flow expanded around the aft portion of the ballute. The flow in the region where the ballute attached to the SRM casing was again largely separated causing a large region of nearly constant pressure.

Pressure contours shown in figure 14 are for three ballute shapes. The ballutes attached to the SRM casing with initial angles of 70°, 75°, and 80°. Increasing initial angle implies increasing ballute size. The pressure contours for the 70° ballute show a separation shock formed just downstream of the SRM expansion shoulder. This shock interacted with the blunt nose shock, but only a modest pressure increase was realized. The pressure contours for the 75° ballute show that the nearly constant pressure separated region has enlarged. The 75° ballute formed a stronger blunt shock than the 70° ballute. This shock interacted with the bow shock off the nose and produced a small region of high pressure. The pressure contours for the 80° ballute also show a very large separated region, but a stronger shock was produced by this ballute. The interaction of the nose bow shock and the ballute bow shock produced an area of peak pressure that is considerably higher than for the 75° ballute. Also the size of the high pressure region on the surface of the 80° ballute was almost twice that for the 75° ballute.

The C_D produced by these three shapes is shown in figure 15. For the problem considered here, a C_D of around 5 was required. As can be seen in figure 15 , a 75° ballute would produced the desired drag. But also note that an 80° ballute produced a C_D as high as 10 with only a modest increase in size.

Heat transfer rates for these three cases are shown in figure 16. What is important to note here is that for the 75° ballute, which produced the desired amount of additional C_D, the maximum heat transfer rate was less than that found at the stagnation point of the SRM casing. Also, for the 80° ballute case which produced a very high C_D, the maximum heating rate was on the order of that found at the stagnation point of the SRM casing.

X MOMENTUM

CONTOUR LEVELS
200.0000
400.0000
600.0000
800.0000
1000.000
1200.000
1400.000
1600.000
1800.000
2000.000
2200.000
2400.000
2600.000
2800.000
3000.000
3400.000
3800.000
4200.000
4600.000

35.550	MACH
0.00 DEG	ALPHA
3.15x10**2	Re
5.25x10**-3	TIME
146x71	GRID

Figure 14. Pressure contours. (a) 70° ballute.

163

X MOMENTUM

35.550   MACH
0.00 DEG   ALPHA
3.15x10**2   Re
3.54x10**-3   TIME
146x71   GRID

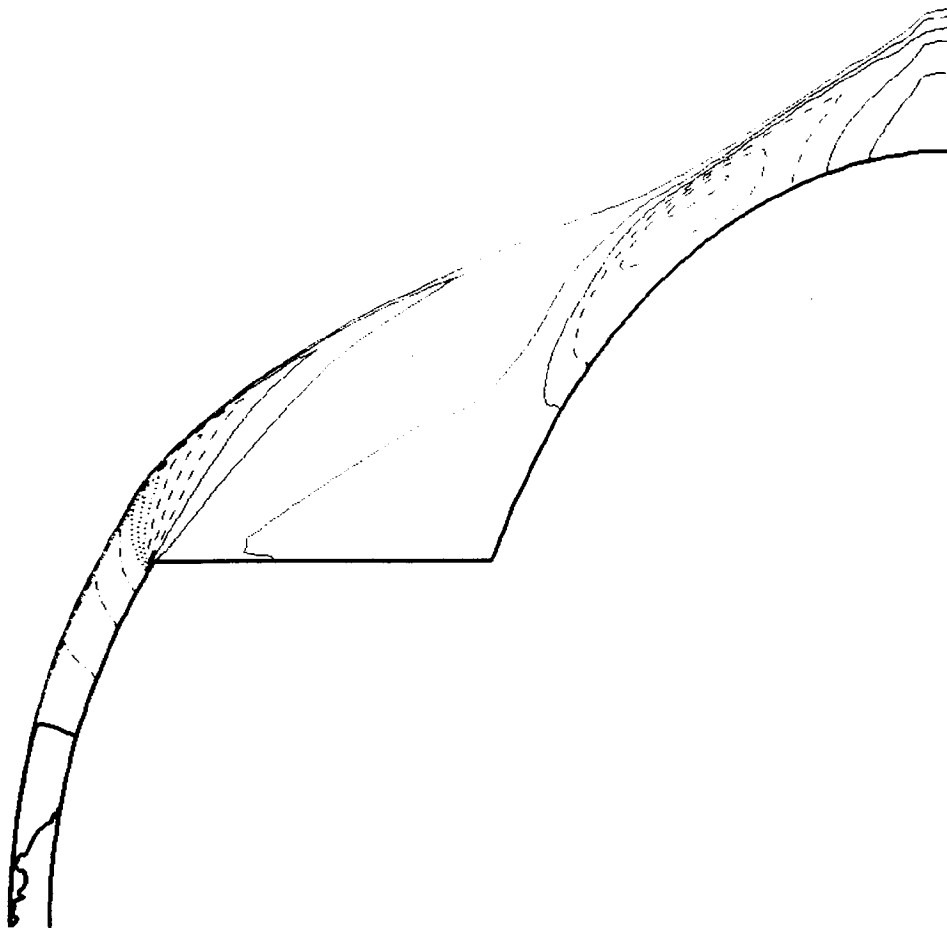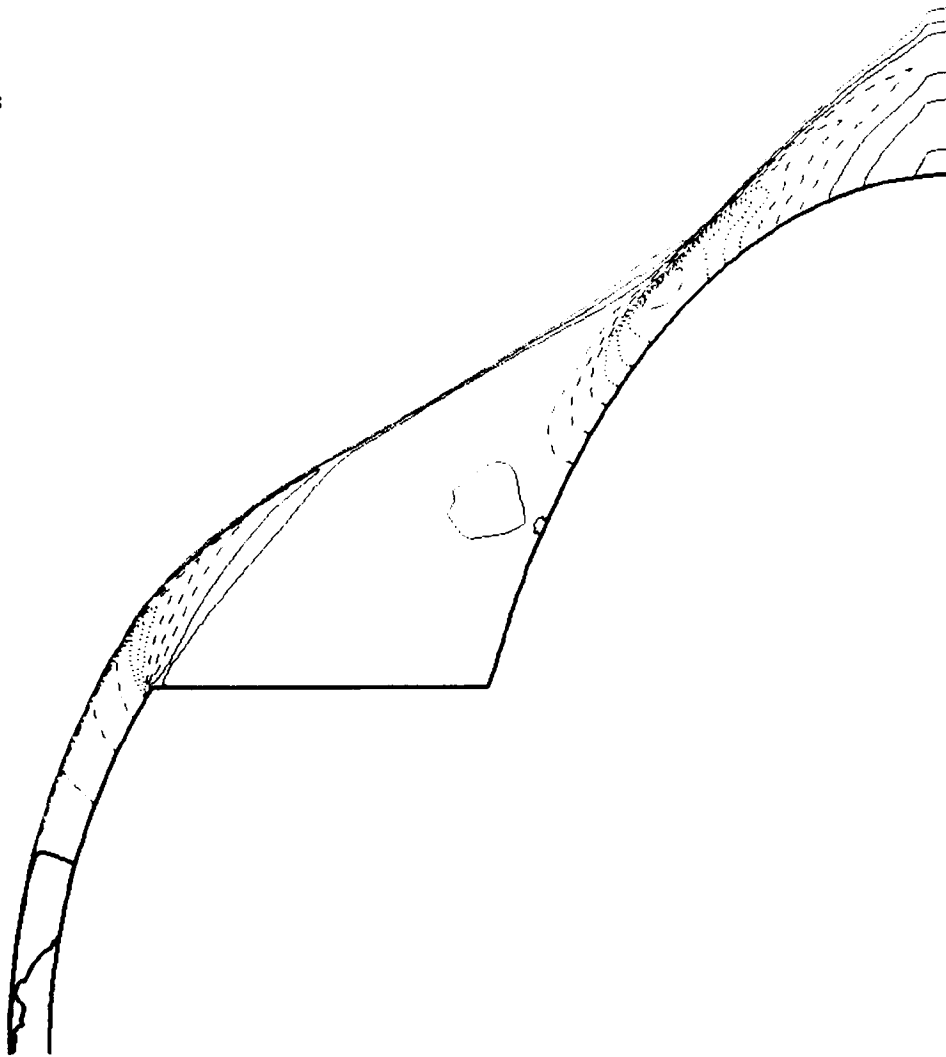Figure 14. Continued. (b) 75° ballute.

164

X MOMENTUM

CONTOUR LEVELS
200.0000
400.0000
600.0000
800.0000
1000.000
1200.000
1400.000
1600.000
1800.000
2000.000
2200.000
2400.000
2600.000
2800.000
3000.000
3400.000
3800.000
4200.000
4600.000

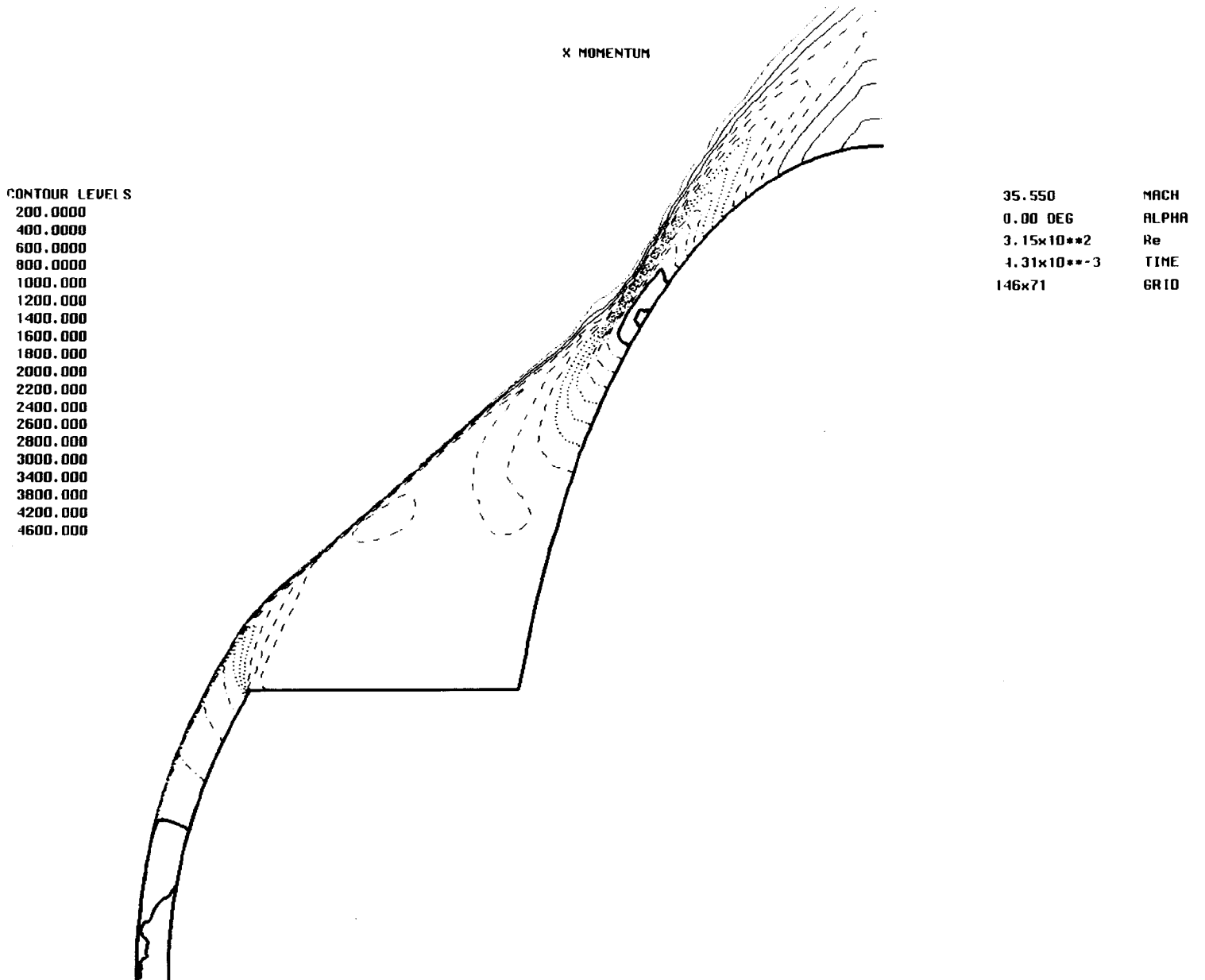| 35.550 | MACH |
0.00 DEG	ALPHA
3.15x10**2	Re
4.31x10**-3	TIME
146x71	GRID

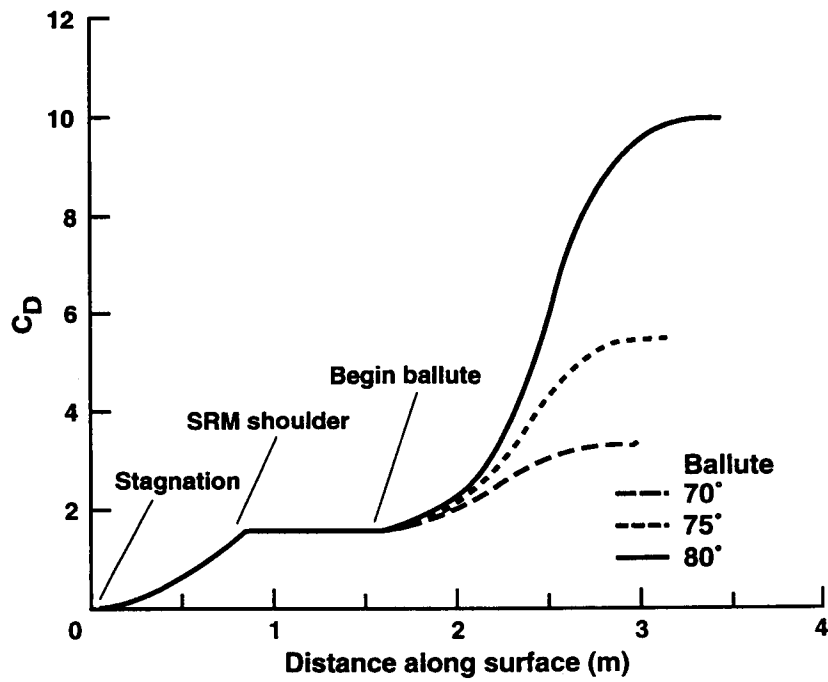Figure 14. Concluded. (c) 80° ballute.
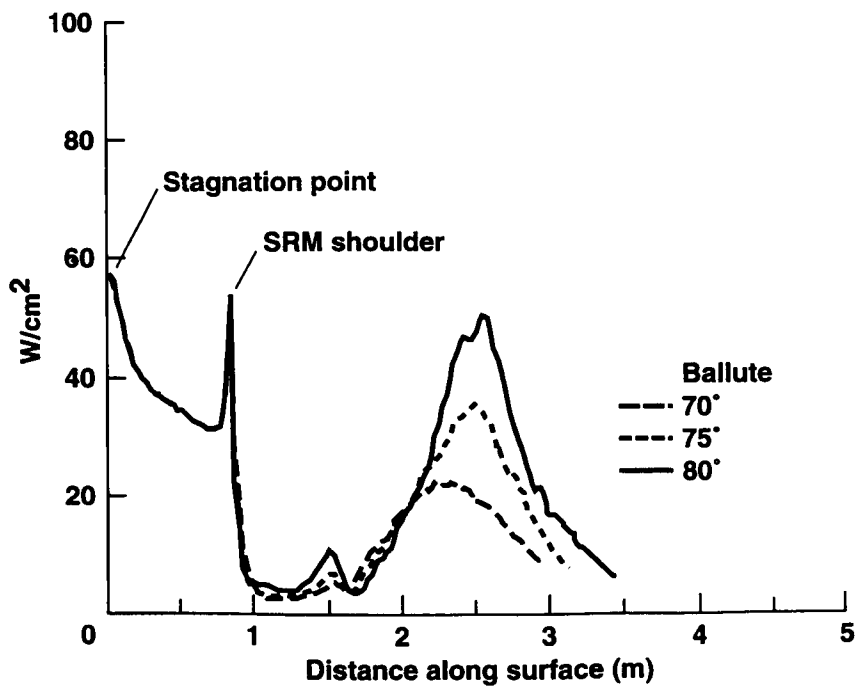
Figure 15. Drag coefficient for ballute.

Figure 16. Heat transfer rats for ballute.

166

A similar type of ballute design was investigated by Wang and Shih (ref. 2). The ballute discussed in reference 2 had a circular cross section. The peak heat transfer rate predicted for the circular cross section ballute was about twice as high as that predicted for the ellipsoidal shapes examined here. Wang and Shih found that a number of existing materials could provide suitable thermal protection for their ballute design. Since neither the heating rates for the flared decelerators nor those for the ballutes exceed those anticipated by Wang and Shih, it is assumed that the same type of thermal protection can be used for the decelerator designs discussed here.

DISCUSSIONS

Comparisons of C_D and heat transfer rates for the flared decelerator and the ballute are shown in figures 17 and 18, respectively. As is indicated in these figures, the ballute is capable of producing a larger amount of drag than the flare for the same amount of heat transfer. Note, however, that the C_D produced by the ballute reaches an asymptotic value, while that for the flare increases linearly as the length of the flare is increased. There are several other considerations which must be addressed before deciding what design is more suited for the SRM mission. First, because the ballute is inflated, it is possible for it to deform in regions of high pressure such as that produced by the shock-shock interaction discussed earlier. These local deformations may cause the SRM/ballute configuration to behave in an unsteady manner. To avoid this problem, the internal pressure of the ballute could be made high enough to make the ballute geometrically stiff. The maximum pressure on the external surface of the 80° ballute was 0.04 atm. Because the maximum external pressure is low, the ballute could be inflated to an internal pressure substantially higher than the maximum external pressure. This would make the ballute essentially stiff. Since the flare decelerator is made of rigid members, local deformations should not be a problem.
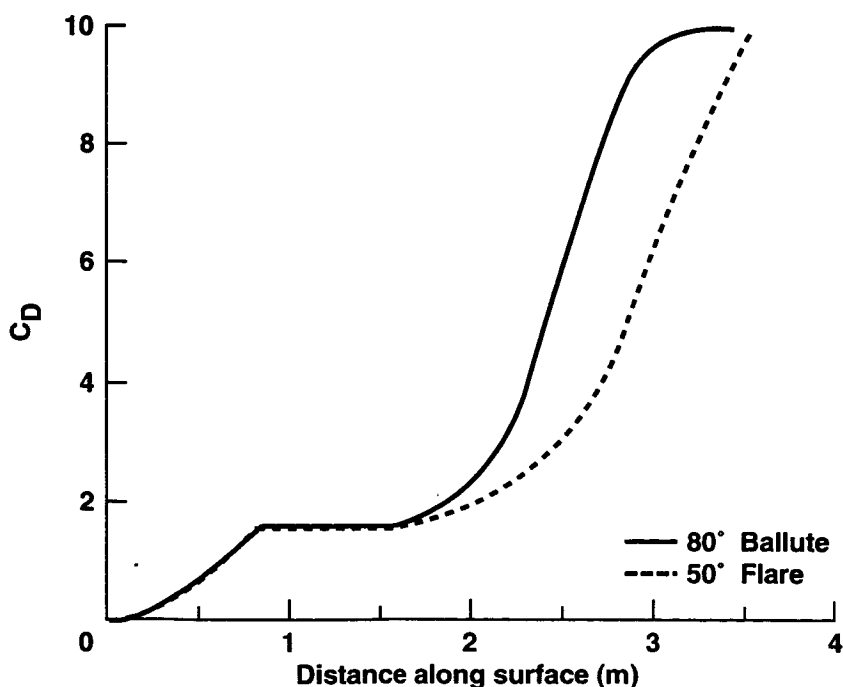

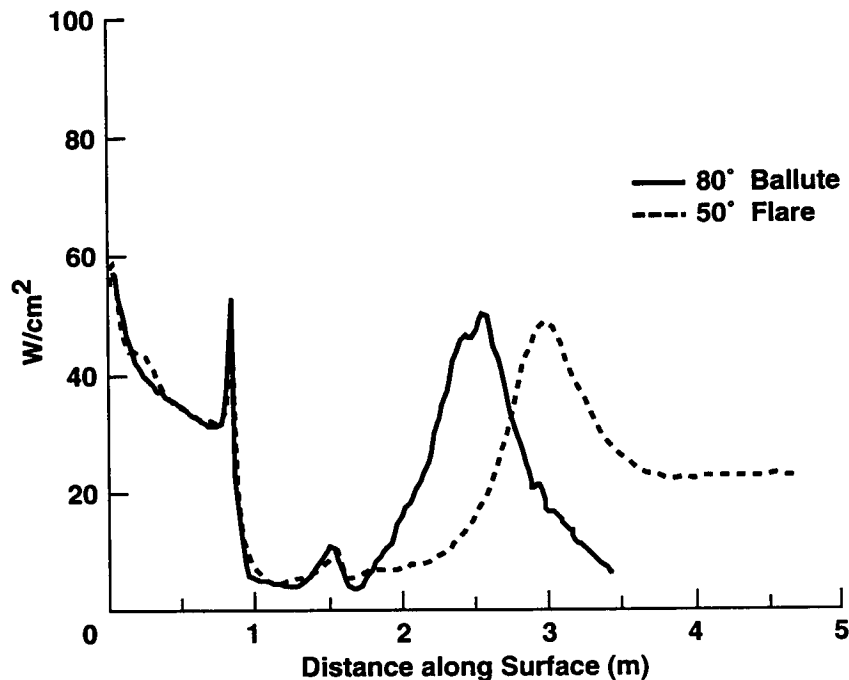Figure 17. Drag coefficient comparison.

Figure 18. Heat transfer rate comparison.

For both the flare and the ballute, the base flow region is not computed. It is likely that the base flow will be unsteady and turbulent. However, the pressure in the base flow region will be very low, so the total drag will not be affected. The heat transfer rates in the base flow region are also expected to be considerably lower than the peak heating rates in the forbody (ref. 11).

Turbulence is neglected in the flowfield computations for the SRM/decelerator. The Reynolds number of the flow is sufficiently low, 2.2×10^4/m, to assume that the flow is laminar. Furthermore, it has been shown that turbulence tends to decrease the size of a separation region for a 2-D compression corner (ref. 9). A reduction in the size of the separated region would cause the amount of drag produced by the decelerator to increase. Therefore, by omitting turbulence, the computations would tend to under predict the drag produced by a decelerator, which is acceptable for design studies. However, if transition did occur, the heat transfer rates in the turbulent region would be higher than if the flow had remained laminar.

It is likely that the SRM/decelerator will not immediately steady out to a zero angle of attack orientation. Instead it will probably go through a transition stage where it will experience a range of orientations at non-zero angles of attack. The peak pressure and heat transfer rates experienced by the decelerators at non-zero angles of attack can be anticipated by looking at zero angle of attack solutions with flare angles larger that the nominal flare angle. For instance, the peak pressure and heat transfer rates experienced by a 50° flare at 10° angle of attack can be estimated by looking at the axisymmetric solution for the 60° flare, figure 11(b). Therefore, by examining higher flare angle solutions, the maximum pressure and heat transfer rates that the decelerator must endure during its mission can be estimated.

168

The ballute and the flare have both desirable and undesirable characteristics as drag decelerators. For instance, the ballute produces a large total drag increase with a relatively low heat transfer rate. However, the efficiency of the ballute is compromised by the large separated region caused by the high angle compression corner. Also, as the flow expands around the downstream end of the ballute the drag increase levels off until it is zero. So the rear end of the ballute, where the local surface is along the freestream direction, does very little to increase the total drag. Since the flare does not have a downstream expansion region, the drag increases linearly with the length of the flare. However, for high flare angles, the heat transfer rates are very high. And for lower flare angles, the length of the flare required to achieve the desired drag increase becomes large. Although the separated regions created by the flares tend to be smaller than for the ballutes, the flares still suffer significant losses due to the separation.

It seems likely that a combination of the flare and ballute geometries could be constructed to take advantage of the desirable characteristics of the separate geometries. An optimization procedure could be performed to produce a geometry that minimizes the separation region, maximizes the total drag increase, and minimizes the maximum heat transfer rate to the decelerator. An optimization study of this sort would be expensive and time consuming in experimental facilities. It would be too costly to perform this sort of study computationally with a full thermo-chemical nonequilibrium solver. However, the computational method used here is very well suited for optimization studies. The computational procedure has about a 10 minute turn around time for each new design, and this time could be considerably reduced with a judicious choice of initial conditions. Furthermore, this procedure could be used to conduct similar design studies for geometries other than hypersonic decelerators. As long as the fluid dynamics are similar and either experimental results for shock shape or CFD results, which take into account real gas effects, for shock shape are available, an appropriate value for effective γ can be chosen. With an appropriate choice of effective γ, the ideal gas code can be used to efficiently study a wide range of vehicle designs.

CONCLUSIONS

This work has shown that, aerodynamically, either the flared decelerator or the ballute decelerator can be used to produce a SRM/decelerator configuration with $\beta = 49$ Kg/m^2 to assure that no atmospheric skip out occurs. The ballute can produce a higher drag increase than the flare for the same amount of surface area and for similar peak heating rates. The heat transfer rates computed for the decelerators can be used to estimate the amount of thermal protection needed to assure decelerator survival for the necessary amount of time.

Employing an ideal gas formulation with an effective γ to compute the pressure field and estimate the heat transfer rates of a hypersonic flowfield with real gas effects has been shown to be successful for preliminary design purposes. The effective γ procedure requires only 5% of the CPU time needed for a full thermo-chemical nonequilibrium solution making this procedure ideal for design studies of this nature.

REFERENCES

1. Aero-Assist Flight Experiment System Requirement Document. MSFC-RQMT-1439-B, NASA Marshall Flight Center, June 1990.

2. Wang, J. A. and Shih, K. C.: Numerical Studies on Inflatable Ballute as an Aerodynamic Decelerator for a Solid Rocket Motor Hypersonic Reentry. AIAA Paper 91-0841, April 1991.

3. Alexander, W.: Summary of the Development Status of Attached Inflatable Decelerators. AIAA Paper 68-929, Sept. 1968.

4. Wyborny, W. and Kabelitz, H.: Comparison of Hypersonic Aerodynamic Deceleration Systems Based on Gun Tunnel Investigations. AIAA Paper 70-1174, Sept. 1970.

5. Palmer, G.: The Development of an Explicit Thermo-Chemical Nonequilibrium Algorithm and Its Application to Compute Three Dimensional AFE Flowfields. AIAA Paper 89-1701, June 1989.

6. Park, C.: Assessment of Two Temperature Kinetic Model for Ionizing Air. AIAA Paper 87-1574, Honolulu, HA, 1987.

7. Candler, G.: The Computation of Weakly Ionized Hypersonic Flows in Thermo-Chemical Nonequilibrium. Ph.D. Dissertation, Stanford University, Palo Alto, CA, 1988.

8. Yates, L. A. and Venkatapathy, E.: Trim Angle Measurements in Free-Flight Facilities. AIAA Paper 91-1632, June 1991.

9. Delery, J. and Coet, M.-C.: Experiments on Shock-Wave/Boundary-Layer Interactions Produced by Two-Dimensional Ramps and Three-Dimensional Obstacles. Workshop on Hypersonic Flows for Reentry Problems, Antibes, France, Jan. 22-26, 1990.

10. Marvin, J. G. and Deiwert, G. S.: Convective Heat Transfer in Planetary Gases. NASA TR R-244, July 1965.

11. Venkatapathy, E. and Feiereisen, W.: Computational Analysis of Plume Induced Separation. AIAA Paper 91-0711, Jan. 1991.

BIOGRAPHY

Susan A. Tokarcik attended the University of Maryland from 1984 to 1988 where she pursued a B.S. in aerospace engineering. During this time she was employed at NASA Goddard through a University of Maryland grant. At Goddard she worked in the geophysics branch as a computer programmer. She also spent one semester and a summer session working as a co-op student at Boeing Helicopter Company in Philadelphia, PA. She continued on at the University of Maryland and received an M.S. in aerospace engineering, specializing in hypersonic aerodynamics, in 1990. While in graduate school, she spent two summers as a visiting student at NASA Ames in the aerothermodynamics branch (RTAC). When she finished her M.S., she was hired by Eloret Institute and now continues her work with RTAC.